UCLA

Title

Light-field tomographic fluorescence lifetime imaging microscopy.

Permalink

Journal

Authors

Ma, Yayao
Park, Jongchan
Huang, Luzhe
et al.

Publication Date

DOI

Light-field tomographic fluorescence lifetime imaging microscopy

Yayao Ma[a,1] (ID), Jongchan Park[a,1] (ID), Luzhe Huang[a,b,c], Chandani Sen[d], Samuel Burri[e] (ID), Claudio Bruschini[e] (ID), Xilin Yang[a,b,c], Qi Cui[a], Robert B. Cameron[f] (ID), Gregory A. Fishbein[g] (ID), Brigitte N. Gomperts[d], Aydogan Ozcan[a,b,c,h] (ID), Edoardo Charbon[e] (ID), and Liang Gao[a,c,2] (ID)

Affiliations are included on p. 11.

Fluorescence lifetime imaging microscopy (FLIM) is a powerful imaging technique that enables the visualization of biological samples at the molecular level by measuring the fluorescence decay rate of fluorescent probes. This provides critical information about molecular interactions, environmental changes, and localization within biological systems. However, creating high-resolution lifetime maps using conventional FLIM systems can be challenging, as it often requires extensive scanning that can significantly lengthen acquisition times. This issue is further compounded in three-dimensional (3D) imaging because it demands additional scanning along the depth axis. To tackle this challenge, we developed a computational imaging technique called light-field tomographic FLIM (LIFT-FLIM). Our approach allows for the acquisition of volumetric fluorescence lifetime images in a highly data-efficient manner, significantly reducing the number of scanning steps required compared to conventional point-scanning or line-scanning FLIM imagers. Moreover, LIFT-FLIM enables the measurement of high-dimensional data using low-dimensional detectors, which are typically low cost and feature a higher temporal bandwidth. We demonstrated LIFT-FLIM using a linear single-photon avalanche diode array on various biological systems, showcasing unparalleled single-photon detection sensitivity. Additionally, we expanded the functionality of our method to spectral FLIM and demonstrated its application in high-content multiplexed imaging of lung organoids. LIFT-FLIM has the potential to open up broad avenues in both basic and translational biomedical research.

fluorescence lifetime imaging microscopy | 3D imaging | light field imaging

Significance

This paper presents a light-field tomographic fluorescence lifetime imaging microscopy (LIFT-FLIM) technique capable of producing three-dimensional (3D) lifetime images in a highly data-efficient manner. In contrast to current FLIM technologies, LIFT-FLIM drastically reduces the required number of scanning steps to capture the same 3D image, leading to an accelerated volumetric frame rate. LIFT-FLIM exhibits immense promise across a range of biomedical applications, including label-free cancer imaging and high-throughput, high-content phenotypic screening.

Fluorescence lifetime imaging microscopy (FLIM) (1, 2) has been extensively employed in a wide spectrum of biomedical applications, ranging from single-cell studies (3–5) to medical diagnosis (6–8). Rather than imaging the time-integrated fluorescent signals, FLIM measures the time-lapse fluorescent decay. Because the lifetime of a fluorophore is dependent on its molecular environment but not on its concentration, FLIM enables a more quantitative study of molecular effects inside living organisms compared with conventional intensity-based approaches.

The FLIM techniques are generally stratified into two categories: frequency-domain FLIM and time-domain FLIM. Frequency-domain FLIM utilizes frequency-modulated light to illuminate the sample, inducing fluorescence that oscillates at the same frequency but with a reduced modulation depth and a phase shift due to the noninstantaneous fluorescence decay (9). To extract the phase shift and modulation depth from the fluorescence signals, frequency-domain FLIM modulates the gain of the camera at the same or slightly different frequency as the excitation light (10–13). The fluorescence lifetime can then be derived from the measured signals by comparing them to a reference fluorophore with a known lifetime. In contrast, time-domain FLIM illuminates the sample with pulsed laser excitation, followed by measuring the fluorescent decay in sequential time channels using an ultrafast detector or detector array. Due to the direct measurement of the fluorescence decay, time-domain FLIM provides more detailed information about decay dynamics than its frequency-domain counterpart. This characteristic becomes especially beneficial when imaging intricate fluorophores exhibiting multiple decay components.

To acquire a two-dimensional (2D) lifetime map, most time-domain FLIM systems scan the sample both in the spatial (14, 15) and temporal domain (16, 17). The spatial and lifetime resolution of the resulting map is determined by the number of scanning steps used in the respective domain. To acquire high-resolution images, conventional time-domain FLIM systems require extensive scanning, which can result in prolonged acquisition times. And this problem becomes more pronounced in three-dimensional

[1]Y.M. and J.P. contributed equally to this work.

[2]To whom correspondence may be addressed. Email: gaol@ucla.edu.

(3D) imaging, as it mandates additional scanning along the depth axis.

The use of single-photon avalanche diode (SPAD) arrays in time-domain FLIM provides a solution to this long-standing problem by enabling parallel measurement of fluorescence decays at multiple image pixels. Moreover, SPAD arrays offer considerably greater sensitivity than conventional gated cameras, making them an excellent choice for low-light imaging applications. A SPAD imager can operate in either time-gated mode or time-correlated single-photon counting (TCSPC) mode, with TCSPC being the preferred detection method for its higher precision, faster speed, and greater sensitivity. However, the native fill factor of 2D SPAD arrays operating in the TCSPC mode is generally low (<10%) (18) due to the physical limitations posed by the inclusion of intricate timing electronics for each pixel. Although the addition of microlenses can recover some of the fill factor loss, this method is effective only for collimated impinging light. In contrast, a linear SPAD array offers a significantly higher fill factor close to 50% (19), which results in a substantially increased light throughput. Moreover, the fabrication cost of a linear SPAD array is much lower than its 2D counterpart, making it more accessible for general labs. Nonetheless, when it comes to high-resolution imaging of a 2D or 3D scene using a linear SPAD array system, the challenge is much like that of point-scanning FLIM—the conventional approach involves scanning the entire field of view or volume using a vast number of steps, which can result in a protracted imaging duration.

To tackle the aforementioned challenges and streamline the acquisition of 3D FLIM data using a linear SPAD array, we devised a computational imaging technique called light-field tomographic fluorescence lifetime imaging microscopy (LIFT-FLIM). Our approach has been only recently made possible by an emerging technique, light-field tomography (LIFT) (20, 21), which is highly efficient in acquiring light-field data for 3D imaging. Sharing its

roots with light-field photography (22–24), LIFT acquires multiple views of a 3D object and determines depth information through disparity analysis. However, rather than directly capturing 2D perspective images, LIFT measures only the en-face projections of the image, thereby transforming 2D perspective images into lines. This allows us to map high-dimensional optical information to a low-dimensional space through pure optical operations. In LIFT-FLIM, we take advantage of this transformation by directly capturing 1D projection images using a linear SPAD array, allowing for 3D fluorescence lifetime imaging with exceptional single-photon sensitivity.

Aside from its 3D imaging capability, LIFT also possesses inherent compatibility with spectral imaging (25). Capitalizing on this feature, we showcased the system's versatility by extending its functionality to include spectral FLIM (sFLIM). We achieved this by dispersing the 1D projection images utilizing a diffraction grating and then feeding the resulting image into a time-gated camera for precise lifetime measurement. This allows for the simultaneous acquisition of 3D FLIM images at multiple wavelengths, making our system a versatile tool for analyzing both lifetime and spectral information. We demonstrated LIFT-FLIM and LIFT-sFLIM on various biological systems, highlighting their potential for high-content multiplexed imaging.

Results

Operating Principle and Characterization. The basic principle of LIFT-FLIM is illustrated in Fig. 1*A*. The core idea is to transform and map 3D image information to a 1D linear sensor through a series of optical operations. A dynamic steering mirror positioned at the image plane tilts the incident 3D scene, producing a perspective view. This perspective image is then rotated using a Dove prism and optically integrated along the horizontal axis with
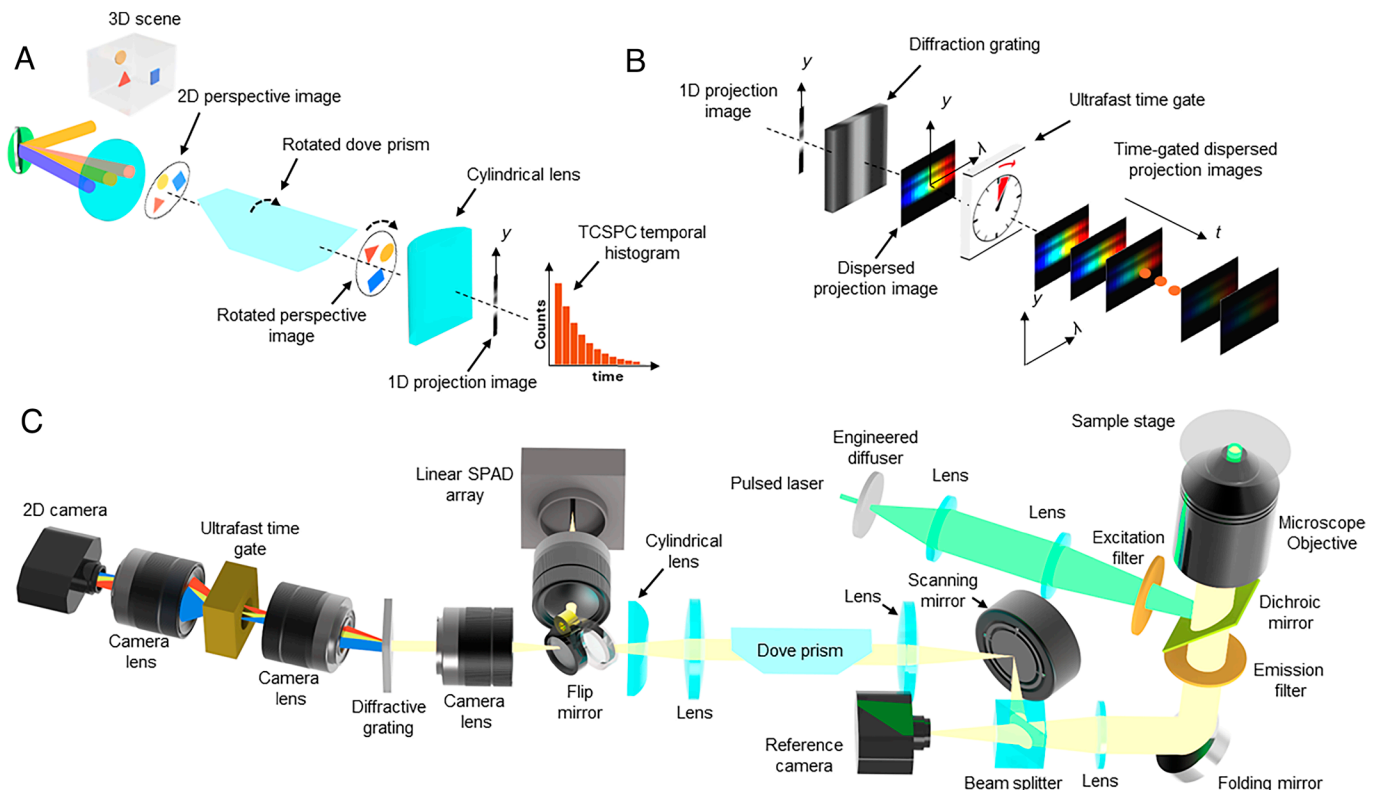
Fig. 1. Optical setup and image formation models. Image formation model of LIFT-FLIM (*A*) and LIFT-sFLIM (*B*). (*C*) System schematics. SPAD, single-photon avalanche diode; TCSPC, time-correlated single-photon counting.

a cylindrical lens. The resulting image is an en-face projection of the perspective view along the orientation set by the Dove prism. This transformed line image can be directly measured by a linear SPAD camera (Fig. 1*A*) or further spectrally dispersed and measured by a time-gated camera (Fig. 1*B*). Measurements are repeated at different steering mirror and Dove prism rotation angles. The schematic of the LIFT-FLIM system is shown in Fig. 1*C*, where the sample is excited using a wide-field epi-illumination configuration. A comprehensive description of the experimental setup is provided in the *Methods* section.

To reconstruct the 3D image, conventional light-field cameras require the acquisition of a comprehensive set of spatial and angular information of a light field, resulting in a significant data load. However, our previous work demonstrated that this acquisition method is inefficient and generates a substantial amount of redundant data (21), which can be reduced by distributing a nonlocal image acquisition process, such as en-face projection measurement, into different views. Moreover, this allows for the measurement of a high-dimensional light field using low-dimensional detectors, which are typically low-cost and feature a higher temporal bandwidth. In LIFT-FLIM, we leverage this advantage and capture only en-face 1D projection images at each scanned subpupil location. Furthermore, we can create an arbitrarily shaped off-focus point spread function (PSF) by strategically shuffling the orientation angles of our projection measurements across various views in a programmed manner (*SI Appendix, Supplementary Note S2*).

We formulate the image formation of LIFT-FLIM using a linear model. For a given perspective image $P_k(u, v)$ at view k ($k = 1, 2, \ldots, K$), the projection measurement along angle θ is

$$f_k^\theta(y) = \mathbf{T}\mathbf{R}^\theta P_k, \qquad [1]$$

where P_k has a size of N^2 ($u = 1, 2, \ldots, N; v = 1, 2, \ldots, N$ is the image dimension in pixels), $\mathbf{T}$ is the en-face projection operator, and $\mathbf{R}^\theta$ is the image rotation operator, which describes the function of the dove prism rotated at $\theta/2$. The number of spatial pixels in the 1D projection image is N ($y = 1, 2, \ldots, N$).

Rather than capturing a complete set of N projection angles at each view, we acquire only a subset of n_k projection angles at view k. This process can be explicitly written as

$$f = \begin{bmatrix} A_1 & \cdots & 0 \\ \vdots & A_2 & \vdots \\ 0 & \ddots & 0 \\ 0 & \cdots & A_k \end{bmatrix} \begin{bmatrix} P_1 \\ P_2 \\ \vdots \\ P_K \end{bmatrix} + \sigma, \qquad [2]$$

Here, $\mathbf{f}$ is a stack of projection measurements (also referred to as a sinogram), and it has a dimension of $N \times N_\theta$, where $N_\theta = \sum_1^K n_k$. $\mathbf{A_k} = \mathbf{T}\mathbf{R_k} = \mathbf{T}\left[\mathbf{R}^{\theta_{k,1}}; \mathbf{R}^{\theta_{k,2}}; \cdots, \mathbf{R}^{\theta_{k,n_k}}\right]$ is a combined function of en-face projection and image rotation operators on perspective image P_k. σ denotes the measurement noise. Because the images from different views capture the same scene, they share a common underlying content (*SI Appendix, Supplementary Note S1*), with only a depth-dependent disparity between any two subaperture images, as shown in *SI Appendix,* Fig. S1. Therefore, the correlation between subaperture images can be modeled by digitally propagating the light field, *i.e.,* the subaperture image P_k at view k can be related to a depth-dependent vectorized image $h(d)$ through an invertible shearing operator $\mathbf{B}_k$ as $P_k = \mathbf{B}_k(d)h(d)$, where $\mathbf{B}_k$ is also a function of depth d (*SI Appendix, Supplementary Note S1*). Accordingly, we transform Eq. **2** to

$$F = \begin{bmatrix} A_1 & \cdots & 0 \\ \vdots & A_2 & \vdots \\ 0 & \ddots & 0 \\ 0 & \cdots & A_k \end{bmatrix} \begin{bmatrix} B_1(d)h(d) \\ B_2(d)h(d) \\ \vdots \\ B_k(d)h(d) \end{bmatrix}$$

$$+ \sigma = \begin{bmatrix} A_1B_1(d) \\ A_2B_2(d) \\ \vdots \\ A_kB_k(d) \end{bmatrix} h(d) + \sigma = F(d)h(\mathrm{d}) + \sigma. \qquad [3]$$

The overall image forward operator $\mathbf{F}(d)$ becomes a function of depth d, which is essential for recovering image $h(d)$ with various focal settings. Noteworthily, although individual P_k is measured at only a subset of projection angles, the underlying image $h(d)$ is measured on a complete angular basis, as $\mathbf{F}(d)$ concatenates image rotation operators across all views.

For direct fluorescence lifetime measurement using a linear SPAD array with TCSPC (Fig. 1*B*), the image formation model is a time-lapse version of Eq. **3**, which can be expressed as

$$\mathbf{f}(t) = \mathbf{F}(d)h(d, t) + \sigma(t), \qquad [4]$$

where $\mathbf{f}(t)$ is a time-lapse sinogram constructed by the projection measurements at the time bin t of a TCSPC temporal histogram.

For spectral FLIM measurement using a gated ultrafast camera (Fig. 1*C*), the image forward model is a function of both time t and wavelength λ:

$$\mathbf{f}(t, \lambda) = \mathbf{F}(d)h(d, t, \lambda) + \sigma(t, \lambda), \qquad [5]$$

where $\mathbf{f}(t, \lambda)$ is a spectrally resolved, time-lapse sinogram constructed by the projection measurements at the gated time t and wavelength λ.

The image reconstruction of LIFT-FLIM and -sFLIM involves solving the inverse problems of Eqs. **4** and **5**, respectively. Like standard computed tomography, this can be accomplished through simple inverse Radon transform or more advanced optimization algorithms like a Fast Iterative Shrinkage-Thresholding Algorithm (FISTA) (26, 27). We depict the workflow for processing the light-field data, such as image refocusing, extending the depth of field, and rendering a 3D image in *Methods*.

It is noteworthy that LIFT-FLIM acquires data in a compressed manner, reducing the number of projections required for image reconstruction. To reconstruct an image with high fidelity, the object must be sparse in specific domains. We analyzed the LIFT-FLIM image reconstruction fidelity in various conditions (*Discussion*).

Akin to conventional light-field cameras, LIFT-FLIM and -sFLIM divide the aperture to extract the depth information. Therefore, they have a reduced lateral resolution (~1.8 μm) compared with the native diffraction-limited resolution of the objective lens (*SI Appendix,* Fig. S2). To improve the quality of the reconstructed images, we developed a deep-learning-based image enhancement neural network (28–30) (Fig. 2). The input to the neural network consists of reconstructed LIFT depth images, a diffraction-limited reference image captured at the depth zero, and digital propagation matrices (DPMs), which represent the axial distance from the reference image plane to the target plane on a per-pixel basis (31). The neural network then uses a PixelCNN++ architecture (32) to generate high-resolution outputs at corresponding depths. With DPMs, the neural network effectively enhances the image quality by reducing out-of-focus blur and refocusing artifacts usually observed in images captured by light-field cameras with limited angular sampling rates.
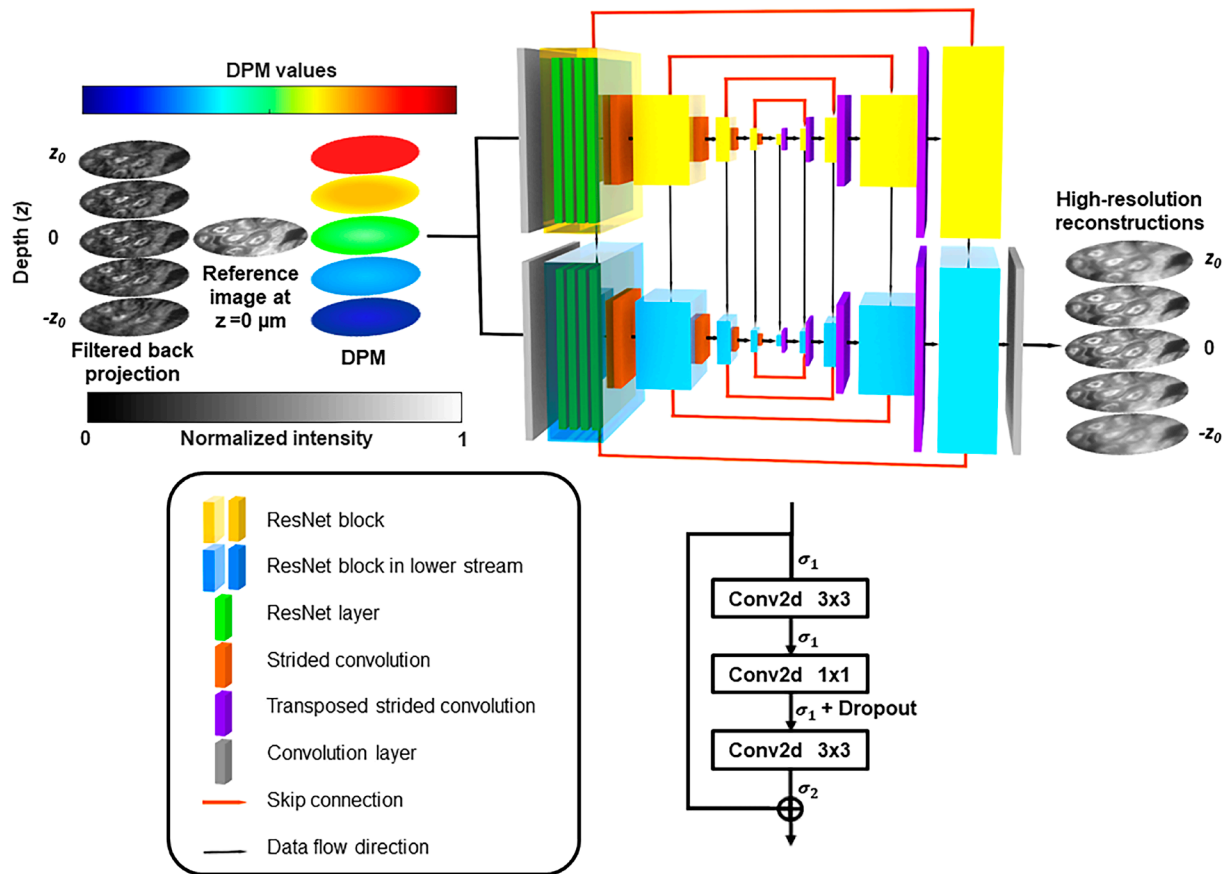
Fig. 2. Deep-learning-based image enhancement neural network. The network consists of two down- and up-sampling streams. Each stream has five ResNet blocks in both down-sampling and up-sampling paths. Each ResNet block contains four ResNet layers, and each ResNet layer has two 3 × 3 convolutional layers and one 1 × 1 convolutional layer, as indicated in the bottom right panel. Strided convolutional layers were added between the two adjacent ResNet blocks to halve the spatial dimensions in the down-sampling path, and conversely transposed strided convolutional layers were utilized to implement up-sampling in the up-sampling path. The spatial dimensions of the ResNet blocks in the sampling streams from left to right are 256 × 256, 128 × 128, 64 × 64, 32 × 32, 16 × 16, 32 × 32, 64 × 64, 128 × 128, and 256 × 256. The central 16 × 16 ResNet blocks are shared by the down- and up-sampling streams. Skip connections connect each ResNet block in the down-sampling path with its counterpart block in the up-sampling path. The inputs to the network include LIFT refocused depth image stack using filtered back projection from depth $-z_0$ to depth z_0, reference image captured at depth zero, and a DPM stack. The output is a high-resolution image stack at the corresponding depths. DPM: digital propagation matrix. σ_1, σ_2: activation functions. Conv2d: convolution 2D.

Further details about the network can be found in *SI Appendix, Supplementary Note S10*. The axial resolution, determined by the NA of the objective lens and the number of views acquired, was measured to be ~3.0 μm for point objects (*SI Appendix,* Fig. S2). The temporal resolutions of LIFT-FLIM and -sFLIM depend on the characteristics of the image sensor. For example, using a linear SPAD array provides a temporal resolution of 50 ps with TCSPC (33), whereas using a gated ultrafast camera yields a temporal resolution of 70 ps.

LIFT-FLIM of Mixed Fluorescent Beads. We validated the 3D lifetime imaging performance of LIFT-FLIM on fluorescent beads. We mixed three types of fluorescent beads with lifetimes of 1.5 ns, 3.4 ns, and 4.0 ns, respectively, in an agarose gel. We simultaneously excited the beads using a filtered supercontinuum laser and imaged the fluorescence using LIFT-FLIM with a linear SPAD array. Moreover, we captured the ground-truth intensity images (Fig. 3A) at depths from -8 μm to 8 μm using a reference camera by mechanically scanning the microscope's focus.

To compare LIFT-FLIM images with the ground-truth images obtained, we summed the signals at all time bins in the TCSPC temporal histogram and reconstructed the time-integrated images at the corresponding depths (Fig. 3B). The resulting images exhibit a high degree of similarity to the ground-truth images, demonstrating the system's numerical refocusing capability. We further

generated the time-lapse LIFT-FLIM images and computed the average lifetime at each image pixel using monoexponential curve fitting (Fig. 3C). Three representative fluorescence decays reconstructed at beads' locations are shown in Fig. 3D. The derived fluorescence lifetimes are consistent with the beads' specifications. Furthermore, we generated a histogram of the lifetimes of all pixels at depth zero (Fig. 3E). This histogram displays three distinct peaks that correspond to the lifetimes of three different types of fluorescence beads. This observation supports the reliability and accuracy of our lifetime measurement.

LIFT-FLIM of a Mouse Kidney Tissue Section. We tested LIFT-FLIM on a standard biological sample (a mouse kidney section, FluoCells™ Prepared Slide from ThermoFisher) and demonstrated its capability in lifetime unmixing. The sample was stained with Alexa Fluor 488 wheat germ agglutinin (WGA) for labeling cell membrane and Alexa Fluor 568 phalloidin for labeling filamentous actin (F-actin). These two fluorophores have distinct but close fluorescence lifetimes (Alexa Fluor 488, 2.6 ns *vs.* Alexa Fluor 568, 2.9 ns). The fluorescence intensity image captured at the focal plane by the reference camera is shown in Fig. 4A. The refocused LIFT-FLIM fluorescence lifetime images at representative depths are displayed in Fig. 4B. Fig. 4C shows the fluorescence decay curves measured at two fluorophore locations, and Fig. 4D shows the histogram of all pixels' lifetimes
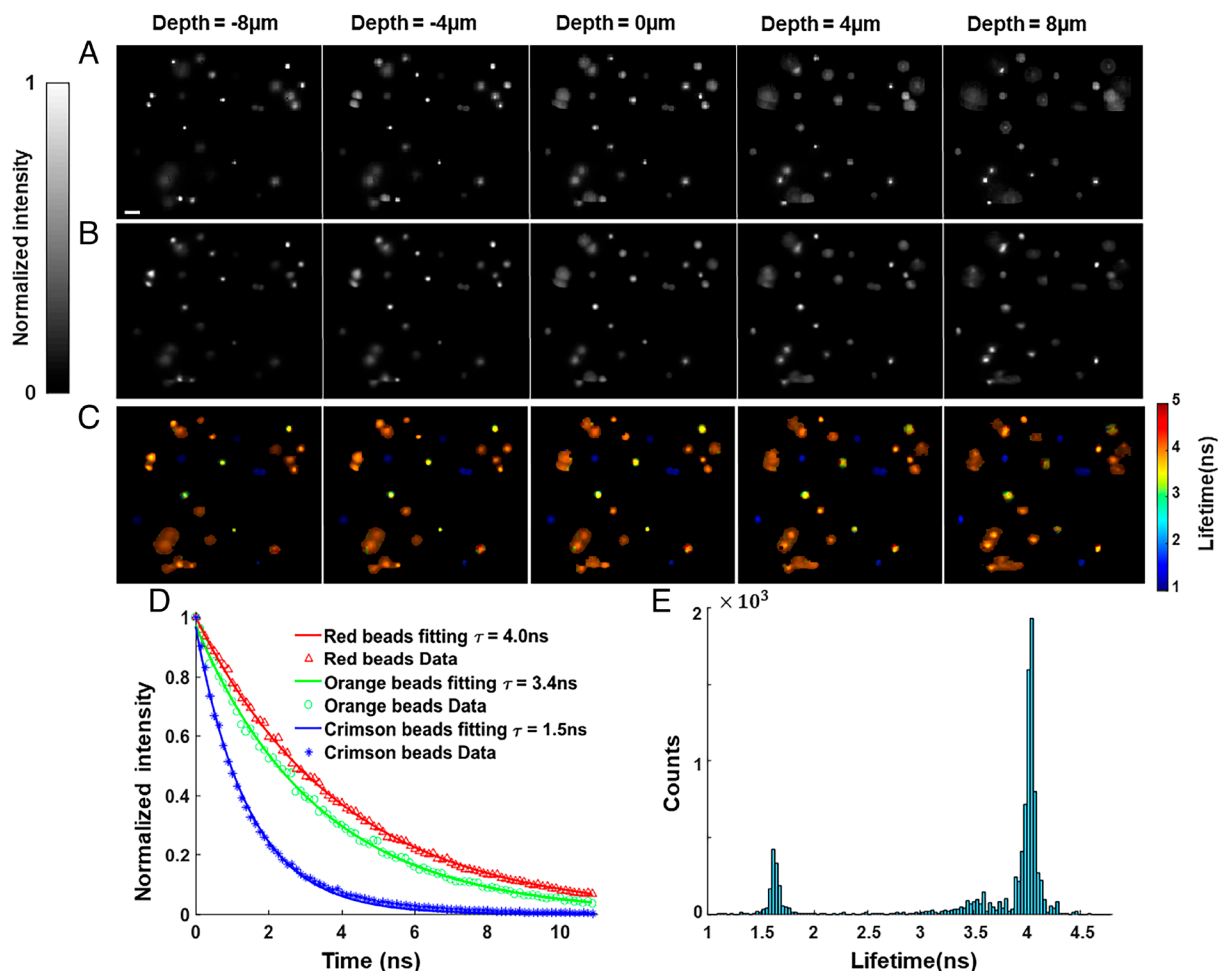
Fig. 3. LIFT-FLIM of mixed fluorescent beads. (*A*) Reference intensity images at depths of −8 μm, −4 μm, 0 μm, 4 μm, and 8 μm. (*B*) Time-integrated LIFT-FLIM images at the corresponding depths. The refocusing to continuous depths is visualized in Movie S1. (*C*) Lifetime images at the corresponding depths. (*D*) Fluorescence decay curves at representative beads' locations. (*E*) Histogram of pixel lifetimes at depth zero (Scale bar, 20 μm.) Data acquisition time: 18 s. Total number of projection angles: 45.

at depth zero, where the two peaks indicate the two underlying lifetime components.

Next, we applied an unsupervised phasor approach (34, 35) to the fluorescence lifetime data and calculated the probability of each pixel belonging to a specific lifetime component cluster. Fig. 4*E* displays the phasor plot for the fluorescence lifetime image at depth zero, with each data point color-coded to represent its corresponding probability and overlaid with probability contour lines. We then classified the image pixels in the time-integrated LIFT-FLIM image based on this probability and unmixed the fluorophores into pseudocolored channels. Fig. 4*F* shows a representative unmixed image at depth zero (red channel, phalloidin; green channel, WGA). Repeating this procedure for all depths yields a 3D unmixed image, as shown in Fig. 4*G*.

LIFT-FLIM of a Human Lung Cancer Pathology Slide. We demonstrated LIFT-FLIM in autofluorescence imaging of an unstained human lung cancer pathology slide. Previous studies show that FLIM can access tumor metabolism by imaging endogenous chromophores such as NAD(P)H and FAD, enabling its application in cancer diagnosis and intraoperative surgical guidance (36, 37). Particularly in pathological imaging, FLIM holds great promise as an alternative approach for label-free detection of tissue lesions (8, 9, 38). However, conventional FLIM microscopes with a high collecting NA suffer from a shallow depth of field. When imaging a panoramic FOV through multiple captures and stitching, the

system must mechanically adjust its focus at each position to correct for potential focal drift that can occur during extensive scanning, complicating the imaging procedure. Here, we show that, by using numerical refocusing, LIFT-FLIM enables an extended depth of field and allows for capturing an all-in-focus image without the need for accounting for the focal drift.

We excited the sample at 450 nm and collected the autofluorescence in the range of 490 to 700 nm. The primary endogenous fluorophore that accounts for the fluorescence emission at this wavelength is flavin adenine dinucleotide (FAD). To image a large FOV, we scanned the sample and stitched the images. The resultant fluorescence intensity image captured by the reference camera is shown in Fig. 5*A*, where certain parts of the FOV are blurred due to the focal drift. In contrast, LIFT-FLIM can numerically correct for this defocus error in postprocessing and form an all-in-focus image, as shown in Fig. 5*B*. For quantitative comparison, we plotted signal intensities along a dashed line in Fig. 5 *A-B* and show the results in Fig. 5*C*. The image features appear to have much sharper edges in LIFT-FLIM compared to those captured by the reference camera (~36% reduction in full -width at half maximum). Next, we computed the lifetimes for the stitched all-in-focus LIFT image and presented a lifetime map in Fig. 5*D*. A zoom-in area (Fig. 5*E*) shows a significant level of lifetime heterogeneity. To correlate this observation to the tissue state, we stained an adjacent slide from the same tissue sample using standard hematoxylin and eosin (H&E) and imaged it under a wide-field microscope. After
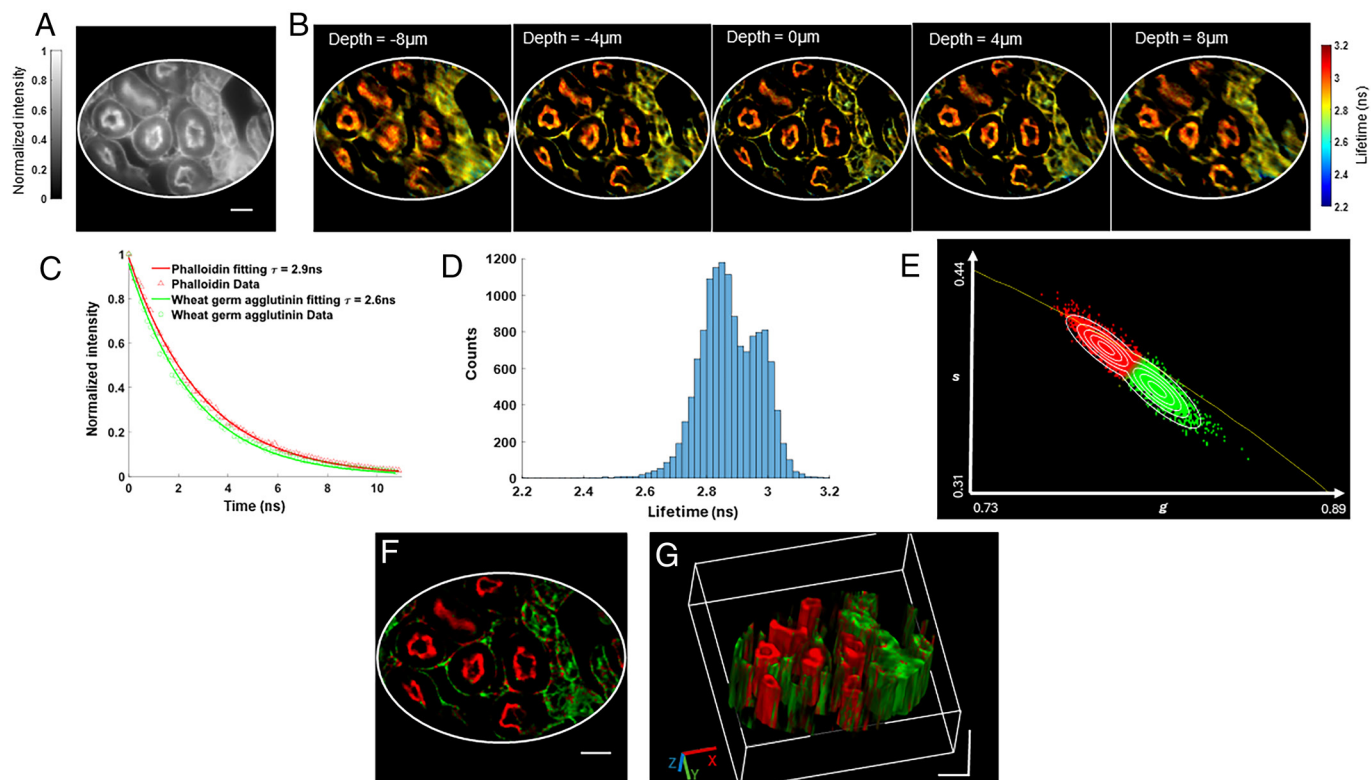
Fig. 4. LIFT-FLIM of a mouse kidney tissue section. (*A*) Reference intensity image at depth zero. (*B*) Reconstructed lifetime images at depths of −8 μm, −4 μm, 0 μm, 4 μm, and 8 μm. The refocusing to continuous depths is visualized in Movie S2. (*C*) Fluorescence decay curves at two representative fluorophore locations. (*D*) Histogram of pixel lifetimes at depth zero. (*E*) Phasor plot. The data points were pseudocolored based on their probability of belonging to a specific cluster (red, phalloidin; green, WGA). The probability contour lines ranging from outer to inner space correspond to values of 0.1, 0.3, 0.5, 0.7, and 0.9. (*F*) Unmixed fluorophore image at depth zero. Red channel, phalloidin. Green channel, WGA. (*G*) 3D visualization of unmixed fluorophores' distribution. Visualization from other perspective angles is provided in Movie S3. Scale bars in all figures: 20 μm. Data acquisition time: 36 s. Total number of projection angles: 90.

the histological image was obtained, a pathologist reviewed it to identify the boundary between the tumor and normal tissue, as illustrated in Fig. 5*F*. Comparing the average pixel lifetimes above (1.9 ± 0.3 ns) and below (2.6 ± 0.4 ns) the annotated boundary (Fig. 5*F*) reveals a significant difference (Fig. 5*G*). The observed reduction in autofluorescence lifetimes in the tumor areas compared to that in the normal tissue is consistent with previous reports (39–41) and may indicate a shift toward glycolysis and cancer metabolism (42). To classify the tissue based on the lifetime, we again applied an unsupervised phasor approach (34, 35) to the fluorescence lifetime data. The resultant phasor plot and classified tissue map are shown in Fig. 5 *H* and *I*, respectively (red channel, tumor; green channel, normal tissue).

LIFT-sFLIM of Lung Organoids. We demonstrated LIFT-sFLIM in 3D multiplex imaging of lung organoids. Organoids, 3D multicellular stem-cell-derived constructs that mimic in vivo tissue, have gained growing interest for modeling tissue development and disease (43–45). Particularly, organoids hold great promise for high-content phenotypic screening because they recapitulate many aspects of parent tissues and can be derived from patient material, rendering them ideal model systems for personalized medicine and drug discovery (46–50).

One primary challenge for high-content phenotypic screening of organoids is extraction of multivariate information from organoids labeled with multiple biomarkers (51–53). Here, we show that, by acquiring both the spectral and lifetime information, LIFT-sFLIM provides a powerful solution to overcome this challenge. We cultured lung alveolar organoids with different combinations of primary healthy human lung fibroblasts and epithelial cells grown on alginate scaffolds that mimic the alveolar microarchitecture (54). We used

the antibodies tabulated in *SI Appendix*, Table S2 and labeled epithelial–mesenchymal transition by α smooth muscle actin (α-sma) expression, ECM deposition by collagen (collagen I) expression, cell apoptosis by SMAD signaling pathway (smad3), and cellular senescence by P16^{INK4A} (p16) expression.

The Fig. 6*A* depicts the fluorescence emission decay curves and spectra of the four fluorophores that were utilized in the secondary antibodies. While the fluorophores AF 532, 546, and 568 have close fluorescence lifetimes, their spectral emission peaks are well separated. On the other hand, AF 546 and AF 555 exhibit significant spectral overlaps but differ in fluorescence lifetimes. The combination of four fluorophores used in this study presents a challenge for conventional imaging techniques. Specifically, neither FLIM nor spectral imaging alone can simultaneously capture and distinguish all four fluorophores. This limitation underscores the need for innovative imaging approaches, such as LIFT-sFLIM, which can integrate both spectral and temporal information to enable reliable separation and quantification of multiple fluorophores in complex biological samples.

Using LIFT-sFLIM, we acquired a five-dimensional (5D) dataset (x, y, z, t, λ) $(x, y, z$, spatial coordinates; t, fluorescence decay time; λ, wavelength). Fig. 6*B* shows the LIFT-sFLIM reconstructed intensity image at depth zero. The wavelength-integrated lifetime image and time-integrated wavelength image at depth zero are shown in Fig. 6 *C* and *D*, respectively. To unmix the fluorophores, we applied a spectral-lifetime phasor approach to the 5D dataset. The resultant color-coded phasor plots in the lifetime and spectral domains are shown in Fig. 6 *E* and *F*, respectively. Consistent with the spectral and lifetime data presented in Fig. 6*A*, our analysis revealed two distinct clusters in the lifetime phasor plot and three distinct clusters in the spectral phasor plot.
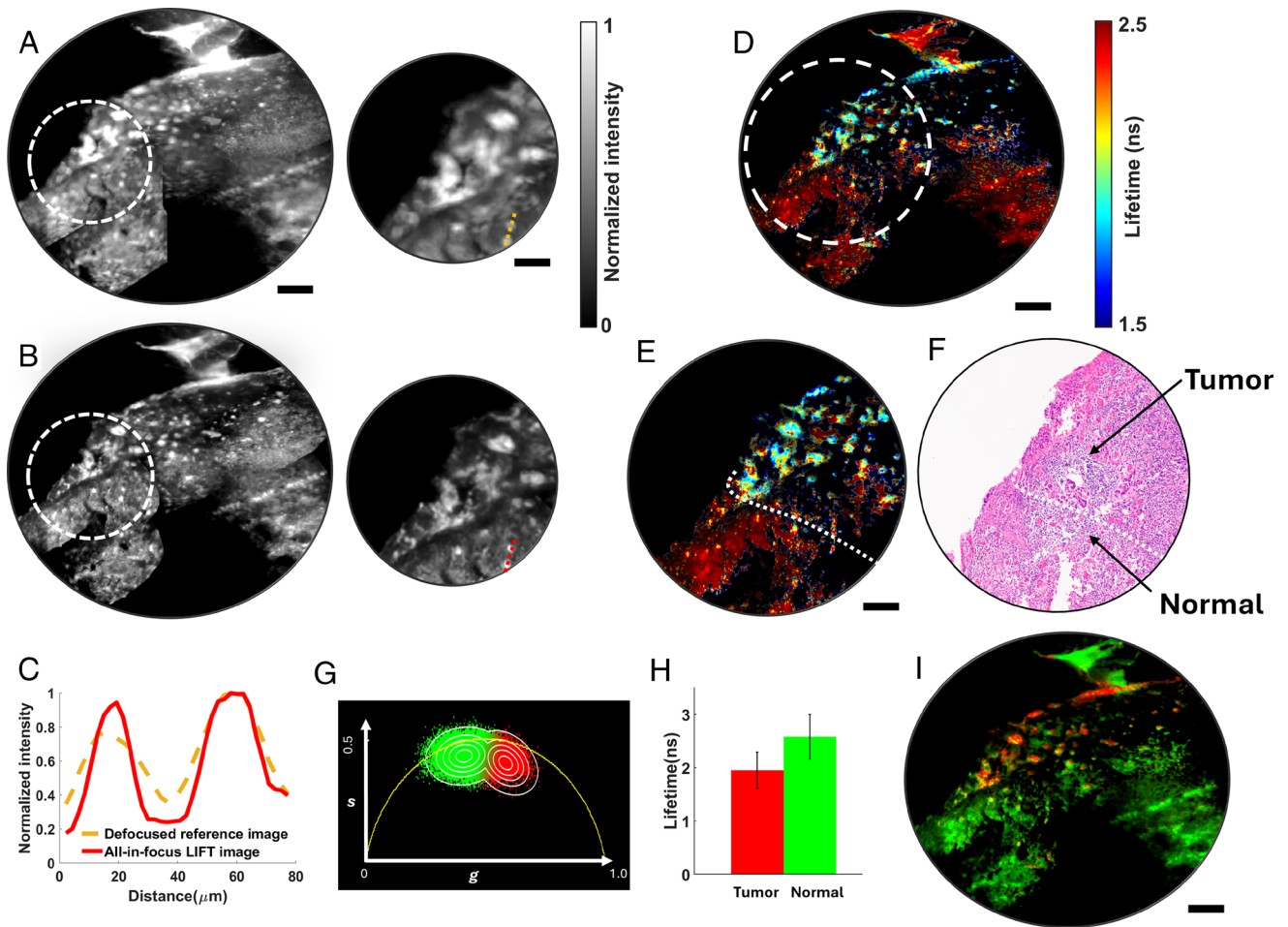
Fig. 5. LIFT-FLIM of a human lung cancer pathology slide. (*A*) *Left* panel: Stitched reference intensity image. *Right* panel: Zoom-in image of the circled area in the *Left* panel. The image is blurred due to focal drift during extensive scanning. (*B*) *Left* panel: Stitched all-in-focus time-integrated LIFT-FLIm image. *Right* panel: Zoom-in image of the circled area in the *Left* panel. (*C*) Intensity profiles of dashed lines in *A* and *B*. (*D*) Stitched all-in-focus lifetime image. The lifetime image is masked with an intensity threshold (*E*) Zoom-in image of the circled area in *D*. (*F*) Hematoxylin and eosin (H&E)-stained image from an adjacent tissue slice. The tumor/normal tissue boundary was identified by a pathologist and annotated with a white dashed line. (*G*) Average pixel lifetimes in the tumor and normal tissues areas in *E*. The SD is shown as error bars. (*H*) Phasor plot. The data points were pseudocolored based on its probability belonging to a specific cluster (Red, tumor; Green, normal). The probability contour lines ranging from outer to inner space correspond to values of 0.1, 0.3, 0.5, 0.7, and 0.9. (*I*) Classified tissue map. Red channel, tumor; green channel, normal. Scale bars in all figures: 100 μm. The data acquisition takes 36 s for each scanned FOV. Total number of projection angles for each scanned FOV: 90.

By combining spectral and temporal information, we separated the fluorophores into four color-coded channels. Representative images at depth zero are shown in Fig. 6*G*. By repeating this procedure at all depths, we generated a 3D color-coded image that depicts the distribution of each fluorophore in the organoid, as shown in Fig. 6*H*.

Discussion

Using LIFT-FLIM for 3D lifetime imaging offers a crucial benefit of reducing the number of scanning steps required compared to traditional point- or line-scanning time-domain FLIM techniques. To produce a 3D image of $N_x \times N_y \times N_z$ voxels, a FLIM system that uses point- or line-scanning requires a total of $N_x \times N_y \times N_z$ or $N_y \times N_z$ (if line scans are done along the y axis) scanning steps, respectively. Here, N_x, N_y, and N_z denote the number of spatial samplings in a 3D space. For simplicity, we consider $N_x = N_y = N$. In contrast, because LIFT-FLIM distributes projection measurements into different views, it demands only N_θ scanning steps, where N_θ is a total number of projection angles. Therefore, LIFT-FLIM reduces the scanning steps required by a factor of $N^2 \times N_z / N_\theta$ or $N \times N_z / N_\theta$ compared to point- or line-scanning systems.

For noncompressive measurement, we set N_θ equal to N. Additionally, as demonstrated in *SI Appendix*, *Supplementary Note S4*, our findings indicate that, in the light-field imaging, the effective number of depth samplings, N_z, equals the number of angular samplings, K. As a result, the scanning reduction factor is either $N \times K$ or K when compared to point- or line-scanning systems. With our current N and K values set at 180 and 15, respectively, the resulting scanning reduction factors are 2,700 and 15 in comparison to point- or line-scanning systems.

Alternatively, like sparse-view computed tomography (55), we can choose an N_θ less than N for compressive measurement. We define a compression ratio (CR) as

$$\text{CR} = N / N_\theta. \quad [6]$$

In the compressive imaging framework, the number of measurements required to reconstruct the image can be substantially reduced. However, the image reconstruction fidelity depends on the CR and the sparsity of the image. Generally, the image must be compressible, so it can be sparsely represented on a certain
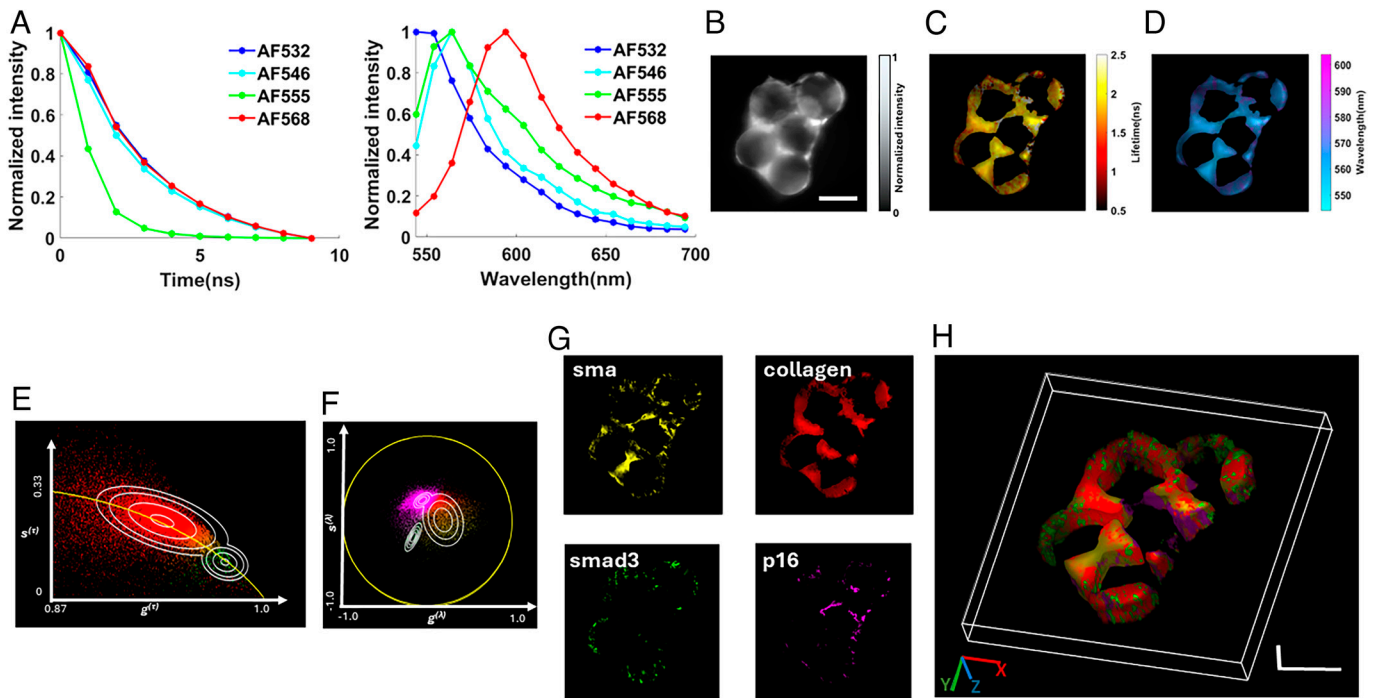
Fig. 6. LIFT-FLIM of lung organoids. (A) Fluorescence decay curves (*Left* panel) and emission spectra (*Right* panel) of the fluorophores used. (*B–D*) Reconstructed LIFT-sFLIM (*B*) intensity image, (*C*) wavelength-integrated lifetime image, and (*D*) time-integrated wavelength image at depth zero. (*E*) Lifetime phasor plot. The data points were pseudocolored based on its probability belonging to a specific cluster (red, sma, collagen, p16; green: smad3). The probability contour lines ranging from outer to inner space correspond to values of 0.2, 0.35, 0.65, and 0.95. (*F*) Spectral phasor plot. The data points were pseudocolored based on its probability belonging to a specific cluster (magenta: collagen, smad3; yellow: sma; green, p16). The probability contour lines ranging from outer to inner space in the magenta and yellow clusters correspond to values of 0.45, 0.65, and 0.85, while the contour lines in the green cluster correspond to values of 0.25, 0.45, 0.65, and 0.85. (*G*) Unmixed component images at depth zero. (*H*) 3D visualization of unmixed fluorophores' distribution in the organoid. Visualization from other perspective angles is provided in Movie S4. Scale bar: 100 µm in all figures. Data acquisition time: 23 s. Total number of projection angles: 90.

basis. Under this condition, a basis-pursuit method reconstructs the image by finding its sparse representation.

To quantify the dependence of the reconstructed image quality on the CR, we adopted the peak signal-to-noise ratio (PSNR) and structural similarity index measure (SSIM) as evaluation metrics. We varied the CR by increasing N_θ and calculated the corresponding PSNRs and SSIMs. *SI Appendix,* Fig. S3 illustrates reconstructions of sparse and complex objects at different CR values. In general, reducing the CR improves both PSNR and SSIM in the reconstructed image. Additionally, our findings suggest that the quality of the reconstructed image is highly dependent on the CR for complex objects, like the lung tumor image displayed in *SI Appendix,* Fig. S3C. In such cases, a lower CR value, less than 4.5, is necessary to achieve high-quality image reconstruction (SSIM ≥ 0.9). Conversely, when imaging a sparse object, such as an USAF resolution target, a CR of 9 is sufficient to recover a high-quality image. Therefore, by adjusting N_θ, LIFT-FLIM can tailor the CR to the complexity of a sample, resulting in effective measurements for a given object.

The Imaging speed of LIFT-FLIM is determined by the total number of projections N_θ acquired and the time duration at each projection. For LIFT-FLIM using a linear SPAD array, the duration at each projection includes both the pixel exposure time and temporal histogram readout time. For LIFT-sFLIM using a gated ultrafast camera, the duration at each projection equals the product of the number of time gates and the camera frame time. Importantly, when imaging simple objects, the system can be operated in the compressive measurement mode, where a reduced N_θ can be acquired to accelerate the imaging speed without compromising the image quality (*SI Appendix,* Figs. S3 and S15).

The spatial resolution of LIFT-FLIM is fundamentally limited by optical diffraction when performing noncompressive measurements.

Due to the division of the aperture, LIFT-FLIM has a lateral resolution of $\lambda f/D$, where λ is the wavelength, f is the focal length of the objective lens, and D is the subaperture diameter associated with a perspective image. Given K views, $D = D_0/\sqrt{K}$, where D_0 is the original aperture of the objective lens. Therefore, the lateral resolution is $\sqrt{K}$ times greater than the native resolution of the objective lens. Although this is a common issue encountered by all light-field cameras, we can mitigate it by acquiring fewer views and increasing the subaperture size to enhance the resolution at the expense of reduced depth accuracy. On the other hand, when performing compressive measurements, the spatial resolution of LIFT-FLIM is practically limited by the CR. While a higher CR is favored in terms of imaging speed, it deteriorates the reconstructed image quality and resolution for complex objects. Hence, selecting an appropriate CR value for a given object involves striking a balance between imaging speed and resolution.

LIFT-FLIM images can be reconstructed and analyzed in real time. For instance, when processing uncompressed measurement data, a simple inverse Radon transform takes about 0.13 s per time bin on an Nvidia RTX3080Ti GPU with CUDA. Subsequently, deep learning enhancement and phasor analysis require 0.079 and 0.024 s, respectively. Parallel computing reduces the total post-processing time to less than 0.3 s.

The light throughput of LIFT-FLIM depends on the subaperture size of a perspective image, the ratio of projection line image width to the detector pixel's size, and the fill factor of the image sensor. As detailed in *SI Appendix, Supplementary Note S3,* the LIFT-FLIM is built on an unfocused light-field imaging configuration, where the projection line width at the image sensor equals to the subaperture diameter, D, multiplying with a pupil demagnification ratio, r. Given the pixel pitch, p, and fill

factor, κ, the percentage of light measured by the image sensor pixel is

$$\zeta_{\text{FLIM}} = \frac{D}{D_0} \times \frac{p\kappa}{Dr} = \frac{p\kappa}{D_0 r}. \qquad [7]$$

Here, D/D_0 describes the light loss due to the view selection during pupil scanning, where D_0 is the original aperture of the objective lens. Therefore, a lower pupil demagnification ratio (*i.e.,* a shorter focal length of the cylindrical lens in Fig. 1*A*) can lead to a higher system light throughput. In our current system, due to use of only off-the-shelf optics and a SPAD array, we have r equal to 0.1, resulting in an overall light throughput of 0.01. To further enhance the system performance, one possible approach is to utilize custom optics that feature a lower pupil demagnification ratio, r, together with a rectangularly shaped SPAD pixel that has a longer pixel pitch, p, in the direction of the projection line width. Alternatively, instead of scanning the pupil to choose the views, it is possible to simultaneously capture all perspective images by employing an array of dove prisms with different orientations, as we have previously demonstrated (25). However, this setup necessitates the use of multiple linear SPAD arrays, each of which measures a projection line image in a synchronized fashion.

On the other hand, for LIFT-sFLIM using a gated ultrafast camera, the light throughput is determined by the subaperture size of a perspective image, the diffraction efficiency of the grating, χ, and quantum efficiency of the gated ultrafast camera, η.

$$\zeta_{\text{sFLIM}} = \frac{D}{D_0} \times \chi \times \eta. \qquad [8]$$

Since $D/D_0 = 1/\sqrt{K}$, where K is the total number of views acquired, Eq. **8** can be rewritten as $\zeta_{\text{sFILM}} = \chi\eta/\sqrt{K}$. Hence, reducing the number of angular samplings can boost the light throughput, but this comes at the cost of decreased depth accuracy. Noteworthily, here the pupil magnification ratio, r, has no effect on the light throughput. Rather, it governs the spectral resolution of the system like in a conventional pushbroom imaging spectrometer (56, 57).

To investigate how the number of photons received at a pixel affects the quality of the reconstructed image, we conducted simulations under a shot-noise-limited condition. Provided that the pixel with the maximum count in the image collects M photons, the corresponding shot noise is $\sqrt{M}$ photons. We introduced photon noise to all pixels in the projection images and reconstructed the images with various values of M, while maintaining a constant number of projections across all data points in the plot. *SI Appendix,* Fig. S4 presents the reconstruction results of a Shepp-Logan phantom under different M values. The results indicate that a larger M (*i.e.,* more photons) can lead to a higher PSNR. For high-quality image reconstruction with a criterion of PSNR ≥ 20 dB (58–60), M must be greater than 64 photons.

A fundamental limit for LIFT-FLIM's acquisition speed is the SPAD sensor's dead time, during which the sensor does not respond to subsequent photons after the initial photon counting event (61). When the photon rate is high, photons arriving within the sensor's dead time are discarded, causing the lifetime decay curve to appear shorter—a phenomenon known as the "pile-up effect." To mitigate this issue and prevent counting loss, we control the excitation intensity at the sample, setting the average photon counting rate at each scanned position to a small fraction (< 10%) of the photodetector's maximum photon counting rate (the inverse of its dead time).

Additionally, the compressed measurement reduces the total number of acquisitions, thereby lowering the light dosage to the sample. This is particularly beneficial for 3D imaging, where conventional point-scanning systems require additional scanning along the depth axis. Moreover, wide-field illumination helps reduce phototoxicity. Previous literature suggests that phototoxicity exhibits a nonlinear dependence on laser peak power (62). By maintaining the same total light dosage, phototoxicity in live cells can be minimized by lowering the peak power and increasing the exposure time (63).

Finally, although LIFT-FLIM offers efficient 3D lifetime image acquisition, it lacks intrinsic optical sectioning like confocal or light sheet microscopes (*SI Appendix, Supplementary Note S5*). Although 3D deconvolution can possibly remove out-of-focus light, this process is sensitive to the signal to noise ratio and persistent shot noise can degrade in-focus image contrast. Neural networks with DPM provide an improved 3D imaging quality but require high-fidelity training dataset. Another solution could be combining LIFT-FLIM with structured illumination like light sheets; however, this approach would entail the need for depth scanning, consequently elongating the overall acquisition timeframe. We demonstrated the enhanced optical sectioning capabilities of our method compared to conventional wide-field imaging by utilizing 3D image reconstruction algorithms. However, this improvement comes at the expense of increased computational burden due to the iterative reconstruction process (*SI Appendix, Supplementary Note S9* and *SI Appendix, Figs. S16–S20*).

Capitalizing on its rapid 3D lifetime acquisition capabilities, LIFT-FLIM can find many applications in biomedical sciences. One specific area is high-throughput label-free metabolic imaging of organoids, where FLIM has a unique advantage in examining endogenous metabolic biomarkers like NAD(P)H and FAD. However, the current FLIM techniques stumble in high-throughput screening due to their slow acquisition speed. LIFT-FLIM can potentially address this challenge by offering a rapid means to evaluate the organoid metabolism in 3D. The technological advancement it affords can expedite endeavors like drug discovery and personalized medicine across diverse fields.

To sum up, we have created a highly data-efficient 3D FLIM technique that relies on LIFT and extended its capabilities to 3D sFLIM. We believe that LIFT-FLIM and -sFLIM will find broad applications in high-throughput and high-content imaging of biological cells and tissues, opening up broad avenues for both fundamental and translational biomedical research.

Methods

Experimental Setup. In a LIFT-FLIM and -sFLIM system, we used an epifluorescence microscope (IX83, Olympus) as the front-end optics and excited the sample with a pulsed laser source (SuperK FIANIUM, FIU-15, NKT Photonics, for LIFT-FLIM; SIRIUS GR-2, Spark Laser, for LIFT-sFLIM). The emitted fluorescence is collected by a microscope objective lens (UPLXAPO60XO, Olympus; UPLXAPO20X, Olympus), and an intermediate fluorescence image is formed at the side image port of the microscope.

To split the light, we employed a beam splitter (BSX16, Thorlabs), which transmits 10% of the light to a reference camera (CS2100M-USB, Thorlabs) and reflects 90% of the light to the LIFT-FLIM camera. We placed a steering mirror (MR-15-30, Optotune) at the intermediate image plane to shift the pupil image.

The fluorescence is then directed through a 4f system, which consists of two lenses (ACT508-250-A and AC254-150-A, Thorlabs) with a focal length of 250 mm and 150 mm, respectively. To rotate the perspective image, we mounted a Dove prism (PS990M, Thorlabs) on a motorized rotation stage (PRM1Z8, Thorlabs) and positioned the assembly at the Fourier plane of the 4f system. We also positioned a cylindrical lens (LJ1095L1-A, Thorlabs, invariant axis along the y-axis) 131 mm after the second lens in the 4f system, which generates a 1D en-face projection

of a perspective image along the y-axis. To locate the projection line image, we identified the line with the smallest width. Additionally, we compensated for the focal shift and spherical aberration introduced by the cylindrical lens by defocusing.

The subsequent system is split into two arms, namely the LIFT-FLIM and LIFT-sFLIM arms. The former employs a linear SPAD array (33), while the latter utilizes a 2D ultrafast time-gated camera (High rate image intensifier, LaVision). To switch the light path between the two arms, we placed a flip mirror (TRF90, Thorlabs; PF10-03-G01, Thorlabs) at the line image plane.

When the mirror is positioned at 1, the fluorescence is directed toward the LIFT-FLIM subsystem through a camera lens (YN100mm F2, YONGNUO) and directly measured by the linear SPAD camera. The linear SPAD camera comprises 256 effective CMOS SPAD pixels with a pitch of 26.2 μm. Operating in the TCPSC mode, the SPAD camera provides a temporal resolution of 50 picoseconds (33). It is connected to a FPGA (Spartan 6, Xilinx) with 64 time-to-digital converters (TDCs) and histogram engines, enabling it to process up to 8.5 giga-photons per second. By rotating the dove prisms in a set of angles at assigned views, we sequentially acquired the 1D en-face projections and constructed a sinogram.

In position 2 of the flip mirror, the emitted fluorescence is directed to the LIFT-sFLIM subsystem. The line image is relayed to the image sensor plane by a pair of camera lenses (YN100mm F2, YONGNUO). To disperse the line image along the x-axis, we positioned a transmission diffraction grating (GT50-03, Thorlabs) at the Fourier plane of the relay system. The resultant dispersed projection image is then sampled in time by an ultrafast time gate and further relayed to a 2D camera (CS2100M-USB, Thorlabs) by a camera lens (YN100mm F2, YONGNUO). By varying the delay between the time gate and the laser reference signal, we acquired a series of time-resolved dispersed projection images. To synchronize the steering mirror, the dove prism rotation stage, the camera, and the laser, we employed a digital delay generator (DG645, Stanford Research Systems). To maximize information content for image reconstruction, we chose the dove prism rotation angles from a set of angles that are evenly spaced in the range of [0, 90°].

To tune the illumination wavelength from the supercontinuum laser, we built a wavelength-selecting module (*SI Appendix*, Fig. S5) using a digital micromirror device (DMD). The collimated white laser beam is first dispersed by a transmission diffraction grating (GT50-03, Thorlabs) and line focused onto the surface of the DMD (DLP LightCrafter 6500, Texas Instruments) through a cylindrical lens (LJ1125L1-A, Thorlabs). The broadband illumination has a line dispersion of 54.4 nm/mm on the DMD surface. The DMD has 1920 × 1080 micromirrors, each of which can be individually tilted ±12° relative to the norm. Each column of the DMD corresponds to a different wavelength with a 0.4 nm/column wavelength resolution. By adjusting the mirror pattern, we can select any desired illumination wavelengths. The laser light of selected wavelengths is then spatially recombined by another identical set of cylindrical lens and diffraction grating and directed toward the LIFT-FLIM subsystem.

When imaging the mixed fluorescence beads and mouse kidney tissue section, we used multiband excitation with two different wavelengths (488 nm and 561 nm) and separated fluorescence from excitation using the combination of a multiband dichroic mirror (ZT405/488/551/647rpc, Chroma) and a multiband emission filter (ZET405/488/561/647 m, Chroma). For imaging the human lung cancer pathology slide, we used 450 nm laser excitation, a 495 nm dichroic mirror (T495lpxr, Chroma), and a long-pass emission filter (ET500lp, Chroma). In the case of lung organoids, we used 532 nm laser excitation, a 532 nm dichroic mirror (ZT532rdc, Chroma), and a long pass emission filter (ET542lp, Chroma). The laser fluence at the sample focal plane was approximately 9.9×10^{-7} J/cm², 1.1×10^{-7} J/cm², and 2.9×10^{-3} J/cm² for the mouse kidney section, lung cancer pathology slide, and lung organoid imaging experiments, respectively. These laser fluences were well below the cell damage threshold of 4 J/cm² (64, 65).

Image Reconstruction. To obtain an image of a monochromatic scene at a specific time point and depth from the measurement described by Eq. **3**, we iteratively solve an optimization problem:

$$\arg\min \| f - \mathbf{F}(d)h(d) \|_2^2 + \mu \| \phi(h(d)) \|_1, \qquad [\mathbf{9}]$$

where $\|\cdot\|_2$ denotes the l_2 norm, $\|\cdot\|_1$ denotes the l_1 norm, and $\phi(\cdot)$ is a data regularization term. μ is a hyperparameter that balances the data fidelity and regularization term. In the framework of regularization by denoising (66), $\phi(\cdot)$ is not explicitly specified, and the regularization can be implemented by image denoising methods such as block-matching and 3D filtering (BM3D), total variation

denoisers (67), or a neural network. Besides the iterative method (26, 27), inverse Radon transformation (55) is an alternative approach that could have been used for image reconstruction with lower computational cost. We adopted the neural network approach because of its fast speed and state-of-the-art performance.

We note that when using a neural network to reconstruct the image from the compressed measurement, it is crucial to carefully train the network to avoid data-dependent priors. In our experiments, we trained the neural network using samples with visual appearance resembling those of the test subjects. A mismatch between the training and test dataset can result in hallucinations and other artifacts.

Refocusing and Extending the Depth of Field. A light field acquired by conventional light-field cameras can be parameterized by the aperture plane (u, v) and the image plane (x, y). Indexing view k as (u_k, v_k), the image $P_k(x, y)$ observed from view k can be related to a reference image feature kernel $h(x, y)$ by

$$p_k(x, y) = h(x - su_k, y - sv_k), \qquad [\mathbf{10}]$$

where s is a depth-dependent shearing parameter (*SI Appendix, Supplementary Note S1*). In conventional light-field imaging, refocusing is performed by shifting and adding the subaperture images (68). Unlike conventional light-field cameras, LIFT-FLIM first rotates a perspective image, followed by transforming the rotated image into a line. Therefore, the depth-dependent shearing must be performed parallel to the projection axis.

For subaperture (u_k, v_k) at the projection angle of θ, the shearing of 1D sub-aperture projection is given by

$$s \cdot u_k \cdot \sin\theta - s \cdot v_k \cdot \cos\theta. \qquad [\mathbf{11}]$$

For numerical refocusing, we applied the correspondent shearing factor to each projection image and updated sinogram for reconstructing the depth image (*SI Appendix, Supplementary Note S1*).

Extending the depth of field can be achieved through a similar approach to conventional light-field imaging, which involves refocusing onto different depths, extracting the sharpest feature for each pixel, and assembling an all-in-focus image (69).

System Calibration and Resolution.

Steering Mirror Calibration. To ensure that the scanning range of subapertures fully utilizes the entire aperture of the objective lens, we calibrated the steering mirror's horizontal and vertical tilt angles. Additionally, to optimize the light throughput of each subaperture, we employed a rectangular iris instead of a round one at the aperture stop. The rectangular shape reduces the gaps between adjacent scanned pupil positions and allows more light to pass through a subaperture.

Projection Center Calibration. To calibrate the central position of each projection line image at the sensor plane, we imaged a pinhole (P10D, Thorlabs) positioned at the center of the FOV on the sample stage. We captured images of the pinhole at every projection angle θ and view k and directly localized the center of each line image as $y_{p0}^{(\theta,k)}$ (*SI Appendix, Supplementary Note S1*). Subsequently, we extracted the projection data based on the center location to form a sinogram.

Spectrum Calibration and Resolution. To calibrate the spectral response, we positioned a pinhole (P10D, Thorlabs) at the sample stage and illuminated it with monochromatic light at varied wavelengths. The resulting pixel locations of the projections were recorded and fitted with a linear polynomial, as illustrated in *SI Appendix*, Fig. S7A. The slope of the line determines the spectral sampling of the system, which was calculated to be 0.14 nm. The spectral resolution is defined as the full width at half maximum (FWHM) of the spectral response. A 1 nm bandpass filter (FL532-1, Thorlabs) was used to limit the source wavelength for this measurement, and the raw spectral response is displayed in *SI Appendix*, Fig. S7B, where the FWHM was approximately 9.2 nm. However, this width was a convolution of the geometrical image of the pinhole on the camera (approximately 7 pixels), the bandwidth of the light source (approximately 7 pixels), and the system spectral resolution. The width of a convoluted function (in pixels) can be computed as (69)

$$w(f_1 * f_2 * f_3) = w(f_1) + w(f_2) + w(f_3) - 2, \qquad [\mathbf{12}]$$

where w denotes the width of the function, $*$ denotes the convolution operator, and $f_i (i = 1, 2, 3)$ denotes the individual function in a discrete form. Based on this equation, the width of the spectral resolution on the camera was estimated to be 48 pixels. Given a 0.14 nm spectral sampling, the spectral resolution is 6.6 nm.

Spatial Resolution and Field of View (FOV). To quantify the spatial resolution, we imaged a fluorescence bead with a diameter of 4 μm (F8858, Thermo Fisher), and the raw reconstruction results are presented in *SI Appendix*, Fig. S2 *A–D*, where the lateral and axial full width at half maximum (FWHM) are approximately 4.6 μm and 5.7 μm, respectively. However, the lateral FWHM width was a convolution of the geometric image of the bead on the camera (around 4 pixels) and the system lateral resolution. The width of a convoluted function can be calculated as (70)

$$w(f_1 * f_2) = w(f_1) + w(f_2) - 1, \qquad [\textbf{13}]$$

where w denotes the width of the function, $*$ denotes the convolution operator, and $f_i (i = 1, 2)$ denotes the individual function in a discrete form. Using this formula, the width of the lateral resolution on the camera was calculated to be 2 pixels. Given a 0.9 μm spatial sampling (camera pixel pitch of 26.2 μm divided by system magnification ratio of 29), the lateral resolution was estimated to be 1.8 μm. Similarly, for axial FWHM, the width was a convolution of the bead size and the system lateral resolution. As a result, the axial resolution was estimated to be 3 μm.

We also imaged a group of bars from a USAF resolution target (Group 7 element 3 to 6) along both horizontal and vertical directions and plotted the intensities along the dashed line. The image visibility, defined as $(I_{max} - I_{min})/(I_{max} + I_{min})$, where I is the intensity, was calculated for each group of bars using the peaks and valleys of the intensity. With a visibility threshold of 0.2, the spatial resolution of the bars was determined to be 2.2 μm along both vertical and horizontal directions, indicating an isotropic resolution. The FOV of our system was measured to be 227 μm × 143 μm when using a 60x microscope objective lens (UPLXAPO60XO, Olympus).

Depth Calibration. To calibrate the depth, we utilized a fluorescence bead (C16509, Thermo Fisher) and translated it along the depth axis from -16 μm to 16 μm with a 2 μm step. At each depth, we captured an image and then performed digital refocusing by adjusting the shearing parameter, as described in *Methods: Refocusing and extending the depth of field*. The goal was to identify the shearing parameter that would bring each image into the sharpest focus, which was determined by maximizing a focus measure (*e.g.*, sum of modified Laplacian) for each pixel in the image (20). The best focus shearing parameter at each physical depth was then recorded. The resultant shearing parameter to depth curve was fitted with linear models. With this calibration curve, we can digitally refocus a 3D object to a specific depth using the correspondent shearing parameter. To validate the accuracy of our shearing parameters, we imaged 3D fluorescence beads in an agarose gel and compared LIFT refocusing against the ground-truth depth images captured by a reference camera, as shown in Fig. 3.

Camera Registration. To register the LIFT-FLIM and -sFLIM image with the reference camera, we imaged a 7 by 13 grid pattern. We then extracted the point locations from the reconstructed LIFT-FLIM and -sFLIM images and the reference image and calculated the homography matrix to establish a pixel-to-pixel correspondence between the two cameras. The reprojection error using the homography is less than one pixel, ensuring an accurate registration. This homography matrix is then used to register the LIFT-FLIM and -sFLIM images with reference images for deep learning reconstruction.

Image Stitching. We used a feature-based image stitching algorithm to create a panorama view of the human lung cancer pathology slide from multiple scanned FOVs with overlapping regions. This process involved detecting and matching image features, estimating the geometric transformation between images, and computing the transformation mapped each image onto the panorama. In the process of detecting and matching image features, we identified a minimum of four matching points between consecutive images. This was accomplished either manually or through feature detection algorithms. Subsequently, using these matched points, we calculated the affine transformation matrix for each pair of successive images. For the panorama construction, we designated the initially captured image as the starting point and subsequently aligned and overlaid the other images onto this base to achieve the panoramic view. Moreover, to correct the artifacts in the stitched image caused by connecting the individual images, we applied an intensity averaging technique to the neighboring pixels at the artifact coordinates.

Ground Truth Lung Organoid Imaging using a Confocal Fluorescence Microscope. To show the ground truth locations of individual biomarkers in our lung organoid experiment, we cultured another four sets of lung organoids under the same condition and labeled them with individual fluorophores. We then imaged the organoids using a standard confocal fluorescence microscope (Zeiss LSM 880 Confocal). *SI Appendix*, Fig. S9 presents the color-coded images, which display a similar appearance to our LIFT-sFLIM results.

Sample Preparation.

Mixed fluorescent beads. To create a mixed fluorescent bead sample, we embedded three types of fluorescent beads (F8858, C16509, F8831, Thermo Fisher) into agarose gels. First, we diluted the bead suspensions and sonicated them. Then, we pipetted 10uL of the 4um bead suspension ($\sim 5.7 \times 10^7$ beads/mL), 10μL of the 6 μm bead suspension ($\sim 1.7 \times 10^7$ beads/mL), and 10uL of the 10 μm bead suspension ($\sim 3.6 \times 10^6$ beads/mL) into 10 mL of PBS (10010023, Thermo Fisher) for each type of bead. We mixed 100 μL of the diluted 4 μm bead solution, 100 μL of the diluted 6 μm bead solution, and 100 μL of the diluted 10 μm bead solution to create the final mixed beads solution, which contained approximately 1.9×10^4 4 μm beads/mL, 5.6×10^3 6 μm beads/mL, and 1.2×10^3 10 μm beads/mL.

We prepared the agarose gel by making a 1% [weight/volume] solution of low melting point agarose (A6013, Sigma-Aldrich) in PBS, heating it until it completely dissolved, and cooling it down to approximately 40 °C. We added 2.5 μL of the mixed beads solution to 400 μL of the agarose solution. After sonication, we added a 50 μL drop of the mixture onto a glass bottom dish (P35G-1.5-14-C, Mattek) and allowed it to solidify for a few minutes. Finally, we imaged the ~1 mm thick gel, which contained immobilized fluorescent beads, using the methods described in the main text.

Distal lung organoid preparation. We used a hydrostatic droplet generator to fabricate alginate microbead scaffolds with an average diameter of 100 μm, which mimics the size of pulmonary alveoli. After generating the microbeads, we coated them with collagen I (354249, Corning) and dopamine (H8502, Sigma) in a two-step process to functionalize them for cell culture. The detailed protocol for alginate bead generation and functionalization can be found in (54).

Human primary adult normal lung fibroblasts were isolated from distal lung tissue from a deidentified healthy donor (65-y-old, male, Caucasian, nonsmoker, nonalcoholic) procured from the International Institute for the Advancement of Medicine (IIAM). Human lung tissue was procured under the UCLA-approved IRB protocol #16-000742. The fibroblast (crawled out population) and epithelial (MACS sorted EpCAM$^+$ population) were isolated from the distal tissue and used in this study.

To develop the 3D model, we used a high aspect ratio vessel (HARV) bioreactor vessel (model: RCCS-4H; Synthecon, Houston, Texas) of 2 mL volume and added 0.5 mL of functionalized microbeads and 1.5 mL of media containing a total of 1 million cells (epithelial:fibroblast = 1:1). The vessel was screwed into the bioreactor base and rotated for 48 h to allow optimum cell-bead adherence. After 48 h, the cell-coated bead solution was aliquoted 100μL per well in a glass-bottom 96-well plate (P96-1.5H-N, Cellvis), and the plate was briefly centrifuged (1,000 g × 2 min) to settle the cells/ beads at the bottom of the plate. An additional 150μL media was added to each well. The plate was then kept inside an incubator (37 °C, 5%CO$_2$, 95%RH) and monitored for the formation of self-organized 3D structures. Within the next 72 h, the fully formed 3D coculture organoids with microalveolar structures were observed in each well.

Author affiliations: ᵃDepartment of Bioengineering, University of California, Los Angeles, CA 90095; ᵇElectrical and Computer Engineering Department, University of California, Los Angeles, CA 90095; ᶜCalifornia Nano Systems Institute, University of California, Los Angeles, CA 90095; ᵈUCLA Children's Discovery and Innovation Institute, Mattel Children's Hospital UCLA, Department of Pediatrics, David Geffen School of Medicine, University of California, Los Angeles, CA 90095; ᵉAdvanced Quantum Architecture Laboratory, School of Engineering, Ecole Polytechnique Federale de Lausanne, CH-2002 Neuchâtel, Switzerland; ᶠDepartment of Thoracic Surgery, David Geffen School of Medicine, University of California, Los Angeles, CA 90095; ᵍDepartment of Pathology and Laboratory Medicine, David Geffen School of Medicine at UCLA, Los Angeles, CA 90095; and ʰDepartment of Surgery, David Geffen School of Medicine, University of California Los Angeles, Los Angeles, CA 90095

1. J. Willem Borst, A. J. W. G. Visser, Fluorescence lifetime imaging microscopy in life sciences. *Meas. Sci. Technol.* **21**, 102002 (2010).
2. W. Becker, Fluorescence lifetime imaging – techniques and applications. *J. Microsc.* **247**, 119–136 (2012).
3. P. J. Verveer, F. S. Wouters, A. R. Reynolds, P. I. H. Bastiaens, Quantitative imaging of lateral ErbB1 receptor signal propagation in the plasma membrane. *Science* **290**, 1567–1570 (2000).
4. P. I. H. Bastiaens, T. M. Jovin, Microspectroscopic imaging tracks the intracellular processing of a signal transduction protein: Fluorescent-labeled protein kinase C βI. *Proc. Natl. Acad. Sci. U.S.A.* **93**, 8407–8412 (1996).
5. Y. Sun, R. N. Day, A. Periasamy, Investigating protein-protein interactions in living cells using fluorescence lifetime imaging microscopy. *Nat. Protoc.* **6**, 1324–1340 (2011).
6. P. J. Tadrous *et al.*, Fluorescence lifetime imaging of unstained tissues: Early results in human breast cancer. *J. Pathol.: J. Pathol. Soc. Great Britain Ireland* **199**, 309–317 (2003).
7. Y. Sun *et al.*, Endoscopic fluorescence lifetime imaging for in vivo intraoperative diagnosis of oral carcinoma. *Microsc. Microanal.* **19**, 791–798 (2013).
8. L. Marcu, Fluorescence lifetime techniques in medical applications. *Ann. Biomed. Eng.* **40**, 304–331 (2012).
9. L. Marcu, P. M. W. French, D. S. Elson, *Fluorescence Lifetime Spectroscopy and Imaging: Principles and Applications in Biomedical Diagnostics* (CRC Press, 2014).
10. R. Liu *et al.*, Compact, non-invasive frequency domain lifetime differentiation of collagens and elastin. *Sens. Actuators B Chem.* **219**, 283–293 (2015).
11. R. A. Colyer, C. Lee, E. Gratton, A novel fluorescence lifetime imaging system that optimizes photon efficiency. *Microsc. Res. Tech.* **71**, 201–213 (2008).
12. Y. Zhang *et al.*, Instant FLIM enables 4D in vivo lifetime imaging of intact and injured zebrafish and mouse brains. *Optica* **8**, 885–897 (2021).
13. M. J. Serafino, B. E. Applegate, J. A. Jo, Direct frequency domain fluorescence lifetime imaging using field programmable gate arrays for real time processing. *Rev. Sci. Instrum.* **91**, 033708 (2020).
14. L. A. J. Alvarez *et al.*, SP8 FALCON: A novel concept in fluorescence lifetime imaging enabling video-rate confocal FLIM. *Nat. Methods* **16**, 3 (2019).
15. S. Trautmann *et al.*, Fluorescence lifetime imaging (FLIM) in confocal microscopy applications: An overview. *PicoQuant GmbH* **29**, 12489 (2013).
16. J. Requejo-Isidro *et al.*, High-speed wide-field time-gated endoscopic fluorescence-lifetime imaging. *Opt. Lett.* **29**, 2249–2251 (2004).
17. K. Dowling, S. C. W. Hyde, J. C. Dainty, P. M. W. French, J. D. Hares, 2-D fluorescence lifetime imaging using a time-gated image intensifier. *Opt. Commun.* **135**, 27–31 (1997).
18. C. Bruschini, H. Homulle, I. M. Antolovic, S. Burri, E. Charbon, Single-photon avalanche diode imagers in biophotonics: Review and outlook. *Light Sci. Appl.* **8**, 87 (2019).
19. N. Krstajić, J. Levitt, S. Poland, S. Ameer-Beg, R. Henderson, 256 × 2 SPAD line sensor for time resolved fluorescence spectroscopy. *Opt. Express* **23**, 5653–5669 (2015).
20. X. Feng, L. Gao, Ultrafast light field tomography for snapshot transient and non-line-of-sight imaging. *Nat. Commun.* **12**, 2179 (2021).
21. X. Feng, Y. Ma, L. Gao, Compact light field photography towards versatile three-dimensional vision. *Nat. Commun.* **13**, 3333 (2022).
22. R. Ng, *Digital Light Field Photography* (Stanford University, 2006).
23. G. Wu *et al.*, Light field image processing: An overview. *IEEE J. Sel. Top. Signal Process* **11**, 926–954 (2017).
24. I. Ihrke, J. Restrepo, L. Mignard-Debise, Principles of light field imaging: Briefly revisiting 25 years of research. *IEEE Signal Process Mag.* **33**, 59–69 (2016).
25. Q. Cui, J. Park, Y. Ma, L. Gao, Snapshot hyperspectral light field tomography. *Optica* **8**, 1552–1558 (2021).
26. A. Beck, M. Teboulle, A fast iterative shrinkage-thresholding algorithm for linear inverse problems. *SIAM J. Imaging Sci.* **2**, 183–202 (2009).
27. J. M. Bioucas-Dias, M. A. T. Figueiredo, A new TwIST: Two-step iterative shrinkage/thresholding algorithms for image restoration. *IEEE Trans. Image Process.* **16**, 2992–3004 (2007).
28. G. Barbastathis, A. Ozcan, G. Situ, On the use of deep learning for computational imaging. *Optica* **6**, 921–943 (2019).
29. H. Wang *et al.*, Deep learning enables cross-modality super-resolution in fluorescence microscopy. *Nat. Methods* **16**, 103–110 (2019).
30. Y. Rivenson *et al.*, Deep learning microscopy. *Optica* **4**, 1437–1443 (2017).
31. Y. Wu *et al.*, Three-dimensional virtual refocusing of fluorescence microscopy images using deep learning. *Nat. Methods* **16**, 1323–1331 (2019).
32. T. Salimans, A. Karpathy, X. Chen, D. P. Kingma, Pixelcnn++: Improving the pixelcnn with discretized logistic mixture likelihood and other modifications. arXiv [Preprint] (2017). https://doi.org/10.48550/arXiv.1701.05517 (Accessed 4 February 2024).
33. C. Bruschini *et al.*, "LinoSPAD2: A 512x1 linear SPAD camera with system-level 135-ps SPTR and a reconfigurable computational engine for time-resolved single-photon imaging" in *Quantum Sensing and Nano Electronics and Photonics XIX* (SPIE, 2023), pp. 126–135.
34. L. Scipioni, A. Rossetta, G. Tedeschi, E. Gratton, Phasor S-FLIM: A new paradigm for fast and robust spectral fluorescence lifetime imaging. *Nat. Methods* **18**, 542–550 (2021).
35. A. Vallmitjana, B. Torrado, E. Gratton, Phasor-based image segmentation: Machine learning clustering techniques. *Biomed. Opt. Express* **12**, 3410–3422 (2021).
36. M. C. Skala *et al.*, In vivo multiphoton microscopy of NADH and FAD redox states, fluorescence lifetimes, and cellular morphology in precancerous epithelia. *Proc. Natl. Acad. Sci. U.S.A.* **104**, 19494–19499 (2007).
37. A. J. Walsh *et al.*, Optical metabolic imaging identifies glycolytic levels, subtypes, and early-treatment response in breast cancer. *Cancer Res.* **73**, 6164–6174 (2013).
38. R. Datta, T. M. Heaster, J. T. Sharick, A. A. Gillette, M. C. Skala, Fluorescence lifetime imaging microscopy: Fundamentals and advances in instrumentation, analysis, and applications. *J. Biomed. Opt.* **25**, 71203 (2020).
39. M. Wang *et al.*, Rapid diagnosis and intraoperative margin assessment of human lung cancer with fluorescence lifetime imaging microscopy. *BBA Clin.* **8**, 7–13 (2017).
40. Q. Wang *et al.*, A layer-level multi-scale architecture for lung cancer classification with fluorescence lifetime imaging endomicroscopy. *Neural. Comput. Appl.* **34**, 18881–18894 (2022).
41. S. E. Fernandes *et al.*, S99 Fluorescence-lifetime imaging: a novel diagnostic tool for suspected lung cancer. *Thorax* **76**, A63.2–A64 (2021).
42. M. G. Vander Heiden, L. C. Cantley, C. B. Thompson, Understanding the Warburg effect: the metabolic requirements of cell proliferation. *Science* **324**, 1029–1033 (2009).
43. M. Hofer, M. P. Lutolf, Engineering organoids. *Nat. Rev. Mater.* **6**, 402–420 (2021).
44. J. Drost, H. Clevers, Organoids in cancer research. *Nat. Rev. Cancer* **18**, 407–418 (2018).
45. F. Schutgens, H. Clevers, Human organoids: Tools for understanding biology and treating diseases. *Annu. Rev. Pathol. Mech. Dis.* **15**, 211–234 (2020).
46. I. Lukonin, M. Zinner, P. Liberali, Organoids in image-based phenotypic chemical screens. *Exp. Mol. Med.* **53**, 1495–1502 (2021).
47. H. Renner *et al.*, A fully automated high-throughput workflow for 3D-based chemical screening in human midbrain organoids. *Elife* **9**, e52904 (2020).
48. E. Driehuis, K. Kretzschmar, H. Clevers, Establishment of patient-derived cancer organoids for drug-screening applications. *Nat. Protoc.* **15**, 3380–3409 (2020).
49. Y. Du *et al.*, Development of a miniaturized 3D organoid culture platform for ultra-high-throughput screening. *J. Mol. Cell Biol.* **12**, 630–643 (2020).
50. T. Takahashi, Organoids for drug discovery and personalized medicine. *Annu. Rev. Pharmacol. Toxicol.* **59**, 447–462 (2019).
51. S. M. Czerniecki *et al.*, High-throughput screening enhances kidney organoid differentiation from human pluripotent stem cells and enables automated multidimensional phenotyping. *Cell Stem. Cell* **22**, 929–940 (2018).
52. I. Lukonin *et al.*, Phenotypic landscape of intestinal organoid regeneration. *Nature* **586**, 275–280 (2020).
53. T. Zhou *et al.*, High-content screening in hPSC-neural progenitors identifies drug candidates that inhibit Zika virus infection in fetal-like organoids and adult brain. *Cell Stem. Cell* **21**, 274–283 (2017).
54. D. C. Wilkinson *et al.*, Development of a three-dimensional bioengineering technology to generate lung tissue for personalized disease modeling. *Stem. Cells Transl. Med.* **6**, 622–633 (2017).
55. H. Kudo, T. Suzuki, E. A. Rashed, Image reconstruction for sparse-view CT and interior CT–introduction to compressed sensing and differentiated backprojection. *Quant. Imaging Med. Surg.* **3**, 147 (2013).
56. P. Mouroulis, R. O. Green, T. G. Chrien, Design of pushbroom imaging spectrometers for optimum recovery of spectroscopic and spatial information. *Appl. Opt.* **39**, 2210–2220 (2000).
57. P. Z. Mouroulis, M. M. McKerns, Pushbroom imaging spectrometer with high spectroscopic data fidelity: Experimental demonstration. *Opt. Eng.* **39**, 808–816 (2000).
58. T.-Y. Lee, S. D. Lin, Dual watermark for image tamper detection and recovery. *Pattern Recognit.* **41**, 3497–3506 (2008).
59. A. Alfalou, C. Brosseau, N. Abdallah, Simultaneous compression and encryption of color video images. *Opt. Commun.* **338**, 371–379 (2015).
60. C. O. Quero, D. Durini, R. Ramos-Garcia, J. Rangel-Magdaleno, J. Martinez-Carranza, "Hardware parallel architecture proposed to accelerate the orthogonal matching pursuit compressive sensing reconstruction" in *Computational Imaging V* (SPIE, 2020), pp. 56–63.
61. J. Park, L. Gao, Advancements in fluorescence lifetime imaging microscopy Instrumentation: Towards high speed and 3D. *Curr. Opin. Solid State Mater. Sci.* **30**, 101147 (2024).
62. A. Hopt, E. Neher, Highly nonlinear photodamage in two-photon fluorescence microscopy. *Biophys. J.* **80**, 2029–2036 (2001).
63. A. Kiepas, E. Voorand, F. Mubaid, P. M. Siegel, C. M. Brown, Optimizing live-cell fluorescence imaging conditions to minimize phototoxicity. *J. Cell Sci.* **133**, jcs242834 (2020).
64. R. Dixit, R. Cyr, Cell damage and reactive oxygen species production induced by fluorescence microscopy: Effect on mitosis and guidelines for non-invasive fluorescence microscopy. *Plant J.* **36**, 280–290 (2003).
65. X. Yuan *et al.*, Effect of laser irradiation on cell function and its implications in Raman spectroscopy. *Appl. Environ. Microbiol.* **84**, e02508–e02517 (2018).
66. Y. Romano, M. Elad, P. Milanfar, The little engine that could: Regularization by denoising (RED). *SIAM J. Imaging Sci.* **10**, 1804–1844 (2017).
67. U. S. Kamilov, A parallel proximal algorithm for anisotropic total variation minimization. *IEEE Trans. Image Process.* **26**, 539–548 (2016).
68. R. Ng *et al.*, *Light Field Photography with a Hand-Held Plenoptic Camera* (Stanford University Computer Science Tech Report, 2005).
69. Y. Boykov, O. Veksler, R. Zabih, Fast approximate energy minimization via graph cuts. *IEEE Trans. Pattern Anal. Mach. Intell.* **23**, 1222–1239 (2001).
70. A. V. Oppenheim *et al.*, *Signals & Systems* (Pearson Educación, 1997).
71. Y. Ma, Data and code for Light-field tomographic fluorescence lifetime imaging microscopy. Github. https://github.com/iOpticsLab/LIFT-FLIM. Deposited 18 Sep 2023.